The M$_2$ Internal Tide Simulated by a 1/10° OGCM

ZHUHUA LI

Max Planck Institute for Meteorology, and International Max Planck Research School on Earth System Modelling, Hamburg, Germany

JIN-SONG VON STORCH

Max Planck Institute for Meteorology, Hamburg, Germany

MALTE MÜLLER

Norwegian Meteorological Institute, Oslo, Norway

ABSTRACT

Using a concurrent simulation of the ocean general circulation and tides with the $^1/_{10}°$ Max Planck Institute Ocean Model (MPI-OM), known as STORMTIDE, this study provides a near-global quantification of the low-mode M$_2$ internal tides. The quantification is based on wavelengths and their near-global distributions obtained by applying spectral analysis to STORMTIDE velocities and on comparisons of the distributions with those derived by solving the Sturm–Liouville eigenvalue problem. The simulated wavelengths, with respect to both their magnitudes and their geographical distributions, compare well with those obtained by solving the eigenvalue problem, suggesting that the STORMTIDE internal waves are, to a first approximation, linear internal waves satisfying local dispersion relations. The simulated wavelengths of modes 1 and 2 range within 100–160 and 45–80 km, respectively. Their distributions reveal, to different degrees for both modes, a zonal asymmetry and a tendency of a poleward increase with stratification N and the Coriolis parameter f being responsible for these two features, respectively. Distributions of mode 1 wavelengths are found to be determined by both N and f, but those of mode 2 are mainly controlled by variations in N. Larger differences between the STORMTIDE wavelengths and those of the eigenvalue problem occur, particularly for mode 2, primarily in high-latitude oceans and the Kuroshio and Gulf Stream and their extensions.

1. Introduction

Internal tides are internal waves at tidal frequencies that are generated by barotropic tides flowing over rough topographic features in the stratified ocean. Although some uncertainty still exists in the exact amount of the power available for the mixing in the ocean's interior from internal tides, theoretical and numerical models give estimates for the deep ocean in the range of 0.5–0.8 TW for the M$_2$ internal tide and of 0.9–1.4 TW when considering the largest tidal constituents (Egbert and Ray 2000; Simmons et al. 2004a; Müller 2013; Green and Nycander 2013). The state-of-the-art parameterization of mixing as a result of internal tides (e.g.,

St. Laurent et al. 2002; Simmons et al. 2004b; Saenko and Merryfield 2005; Montenegro et al. 2007; Exarchou et al. 2014) considers only 30% of this power, the part related to high-mode internal tides that dissipate locally at the generation sites, whereby leaving the remaining 70%, the part related to low-mode internal tides, unspecified. The dissipation of the low-mode internal tides can provide a substantial amount of mixing energy, in which not only does the energy input matter, but also where the dissipations occur in the vertical (Melet et al. 2013), and thus it is important for maintaining the meridional overturning circulation (Munk and Wunsch 1998). So far, our knowledge about the fate of these waves is still limited. Particularly limited is our knowledge about their spatial distributions and to what extent they are affected by the realistic stratification and eddying ocean circulation. This limitation is partly caused by the sparse direct observations in the ocean's interior (e.g., Polzin

Corresponding author address: Zhuhua Li, Max Planck Institute for Meteorology, Bundesstraße 53, 20146 Hamburg, Germany.
E-mail: zhuhua.li@mpimet.mpg.de

and Lvov 2011). Satellite altimeters are now frequently used to study internal tides on the global scale, but they provide only integrated wave properties in which modes are superposed (Ray and Mitchum 1997). To advance our understanding, concurrent simulation of the ocean circulation and tides is crucial for studying these low-mode internal tides.

Until recently, tidal and nontidal motions in the global ocean have been studied separately. Predicting ocean tides is largely based on two-dimensional shallow-water equations forced by the tidal forcing only, while simulating the ocean circulation is based on three-dimensional primitive equations forced by momentum and buoyancy fluxes at the sea surface without including the tidal forcing. The first attempts to jointly simulate tides and circulations were made with coarse-resolution ocean-only or climate models (Thomas et al. 2001; Schiller and Fiedler 2007; Müller et al. 2010). Hence, these studies emphasized the effects of barotropic tides on the ocean circulation without resolving mesoscale eddies and internal tides. With increasing computer power, eddy-permitting and eddy-resolving simulations have advanced (Masumoto et al. 2004; Maltrud and McClean 2005; von Storch et al. 2012). The HYCOM group (Arbic et al. 2010, 2012) was the first to report on global concurrent simulations of the eddying general circulation and tides. Soon after another concurrent simulation was carried out using the $1/10°$ Max Planck Institute Ocean Model (MPI-OM), known as the STORMTIDE model (Müller et al. 2012). In both the HYCOM and STORMTIDE models, barotropic tides are reasonably well simulated (Arbic et al. 2010; Shriver et al. 2012; Müller et al. 2012, 2014). The simulated internal tides' signatures in the sea surface height compare well with those obtained from the altimetry data (Arbic et al. 2010, 2012; Müller et al. 2012), suggesting that both the HYCOM and STORMTIDE models have skill in simulating the low-mode internal tides.

In the present study, we aim to gain more understanding of the M_2 internal tide simulated by the $1/10°$ STORMTIDE model using the signatures of the low-mode internal tides in baroclinic velocities. The wavelengths are used as a diagnostic tool to quantify the waves and to answer the following questions:

1) Which modes of the M_2 internal tide are simulated in the STORMTIDE model and how consistent are they with the dispersion relation of linear internal waves? What are the properties of the simulated internal tides, for instance, their wavelengths and the respective geographical distributions?
2) What are the relative roles of local stratification N and the Coriolis parameter f in determining these geographical distributions?

To answer the first question, we use the wavenumber spectra to diagnose the wavelengths from baroclinic velocities simulated by the STORMTIDE simulation and compare the result with wavelengths obtained by solving the Sturm–Liouville eigenvalue problem. To answer the second question, we compare the simulated wavelengths with those obtained by keeping either N or f fixed in the eigenvalue problem.

In section 2, the STORMTIDE model is introduced, including a further evaluation of the simulated M_2 internal tide using sea surface height. Section 3 describes methods used to diagnose the wavelengths of the M_2 internal tide, including a discussion of the significances and limits of these methods. Results are discussed in sections 4–6: The kinetic energy of the internal tides simulated by the STORMTIDE model is briefly discussed in section 4. In section 5, we describe the characteristics of the two-dimensional wavenumber spectra and the geographical distributions of the wavelengths deduced from these spectra and compare the result with those obtained by solving the Sturm–Liouville eigenvalue problem. The relative roles of stratification and the Coriolis parameter are examined in section 6. Section 7 presents the concluding remarks.

2. The STORMTIDE model

The STORMTIDE model (Müller et al. 2012) is based on the high-resolution MPI-OM formulated on a tripolar grid and concurrently resolves the ocean circulation and tides. It was developed in the framework of the German consortium project STORM, with an aim towards a coupled high-resolution climate model simulation (von Storch et al. 2012) in which a multidecadal simulation with the NCEP atmospheric forcing has been obtained. Our branch with tides implemented is hence named the STORMTIDE model.

The tripolar MPI-OM uses basically the same physics as its bipolar predecessor (Marsland et al. 2003; Jungclaus et al. 2006). The horizontal resolution is around $1/10°$, about 10 km near the equator and about 5 km and less south of 60°S. In the vertical, it uses the "z coordinate" system; 40 unevenly spaced vertical layers are used with nine concentrating in the first 100 m. The layer thickness varies gradually from 10 m in the upper ocean to 500 m in the deep ocean.

In our study, the STORMTIDE model is forced by the complete lunisolar tidal potential, as calculated from the instantaneous positions of the sun and moon (Müller et al. 2012). This forcing takes implicitly hundreds of tidal constituents into consideration (Thomas et al. 2001). The self-attraction and loading (SAL) effect is parameterized in the same way as in Thomas et al. (2001). The model is
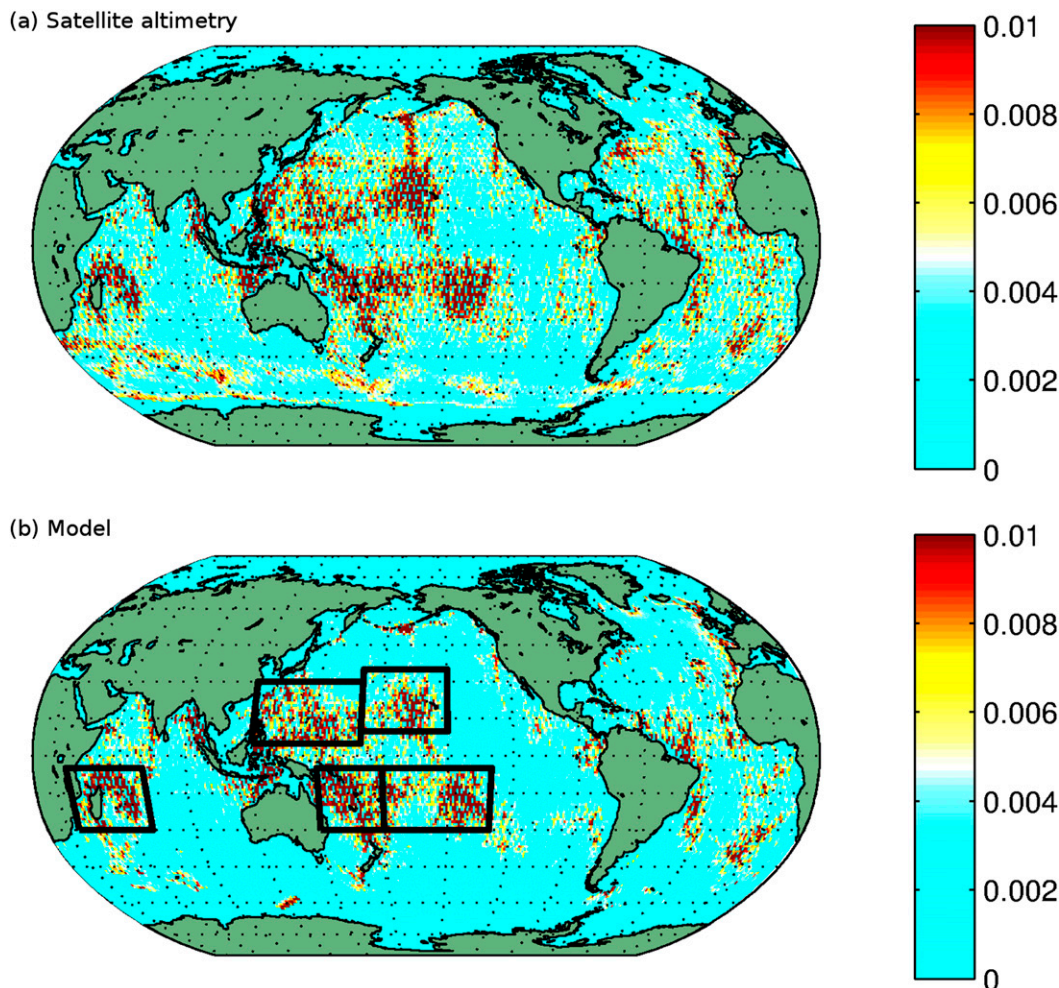
FIG. 1. RMS amplitudes (m) of the M_2 internal tide obtained from (a) the 19-yr satellite altimetry data and (b) the 2-yr hourly sea surface height simulated by the STORMTIDE model. The M_2 tidal signals are high-pass filtered and then binned into $1° \times 1°$ boxes. The black boxes mark the regions of hot spots used in Table 1.

forced at the sea surface by daily climatological wind stresses with a 365-day cycle and a SST and SSS restoration toward the monthly climatological values (Steele et al. 2001), and is integrated over 10 years.

The ability of the STORMTIDE model to simulate realistic barotropic and internal tides was evaluated in Müller et al. (2012). Comparing the simulated barotropic tides with 102 pelagic tidal observations, the STORMTIDE model was able to capture 92.8% of the variance of the barotropic-tide-induced sea surface height for the eight dominant constituents (Müller et al. 2012). In addition, in a model intercomparison (Stammer et al. 2014), the model-simulated barotropic tidal currents of the STORMTIDE model were evaluated. No internal wave drag is implemented in our model approach and instead about 1.1 TW of tidal energy is converted from barotropic to baroclinic tides (Müller 2013), consistent with observational estimates (e.g., Egbert and Ray 2000).

In the following, we further extend the evaluation of the sea surface signatures of the M_2 internal tide in Müller et al. (2012) by incorporating an observational product obtained from 19-yr along-track satellite altimetry [TOPEX, Poseidon, *Jason-1,* and *Jason-2* (TPJ)] data (Cherniawsky et al. 2001; Foreman et al. 2009). Both the M_2 along-track tidal signals obtained from the TPJ data and the model-simulated sea surface height are obtained using a high-pass filter, with a cutoff wavelength of about 350 km, for a removal of the long-wave barotropic tidal signals. The signals are binned, where ocean depths are larger than 1000 m, into $1° \times 1°$ boxes and their root-mean-square (RMS) amplitudes are computed (Fig. 1). Note that since we considered the hourly model-simulated output (1 January–1 February of the ninth simulation year; for details see section 3a), no tidal aliasing (e.g., Zhao et al. 2012) is involved in the simulated data processing, which occurs only in the altimetry data

TABLE 1. The surface signals (cm) of the M_2 internal tide averaged as quantities by RMS over various hot spots regions indicated in Fig. 1. TPJ and STORMTIDE refer to the observations and model simulation, respectively. The last column shows the RMS ratios of the observations to model results.

Region	TPJ	STORMTIDE	Ratio
East of Philippines	0.79	0.74	1.06
Hawaii	0.87	0.60	1.44
Tropical South Pacific	0.97	1.10	0.88
Tropical southwest Pacific	0.86	0.72	1.19
Madagascar	0.85	0.91	0.94

as a result of their poor temporal resolutions. To evaluate the RMS amplitudes in specific hot spots, we choose regions as in Shriver et al. (2012) and indicate them in Fig. 1b. The RMS amplitudes of the model and observations are given in Table 1, along with the RMS ratios of the observations to model results. A large model underestimation is presented in the Hawaii region. In the other regions, the mismatch is less than 20% and reflects a similar quality in simulating the magnitude of internal tides in hot spots regions as in Shriver et al. (2012). Because of the mesoscale contamination (e.g., Shriver et al. 2012) induced by the tidal aliasing in the altimetry data, we can observe large spurious signals in the Gulf Stream and Kuroshio Extensions and the Southern Ocean in the altimetry data. The internal tide beam from the Aleutians is significantly reduced in the model. In general, we conclude that the STORMTIDE model gives us a reasonably good model simulation of internal tides, in regard to what is currently possible in a global model approach.

3. Methods

a. Details in deriving the baroclinic M_2 tidal velocities

For the quantification of the kinetic energy and also for the wavelength analysis of the STORMTIDE data throughout this paper, we use the three-dimensional horizontal M_2 tidal velocities [see Müller et al. (2014) for a detailed description]. They are publicly available (Müller 2012). Because of the huge amount of three-dimensional hourly data used, we limit the data length to be 32 days, which is the minimum requirement for the spectral analysis in order to resolve certain tidal constituents. Using the 32-day model-simulated full zonal and meridional velocities from 1 January to 1 February of the ninth simulation year, we perform the harmonic analysis to derive the amplitudes A_{M_2} and phases ϕ_{M_2} of the full M_2 tidal velocities. Taking the zonal velocities as an example, we describe the full M_2 tidal velocities as

$$u_{M_2}(i,j,k,t) = A_{M_2}(i,j,k)e^{i[2\pi\omega t - \phi_{M_2}(i,j,k)]}, \quad (1)$$

in which i, j, and k are the grid indices in the zonal, meridional, and vertical directions; ω is the M_2 tidal frequency; and t is time. The vertical integration of Eq. (1) gives the barotropic M_2 tidal velocities

$$u_{bt}(i,j,t) = \left[\frac{1}{H}\sum_k A_{M_2}(i,j,k)e^{-i\phi_{M_2}(i,j,k)}\Delta H_k\right]e^{i2\pi\omega t}, \quad (2)$$

in which H is the water depth and ΔH_k is the thickness of the kth layer. The complex baroclinic M_2 velocities are obtained by subtracting the complex barotropic velocities in Eq. (2) from the full velocities in Eq. (1). Denoting the amplitudes and phases of the resulting baroclinic M_2 velocities as $A_{u_{bc}}(i, j, k)$ and $\phi_{u_{bc}}(i, j, k)$, the baroclinic M_2 tidal velocities are given by

$$u_{bc}(i,j,k,t) = u_{M_2}(i,j,k,t) - u_{bt}(i,j,t)$$
$$= A_{u_{bc}}(i,j,k)e^{i[2\pi\omega t - \phi_{u_{bc}}(i,j,k)]}. \quad (3)$$

The amplitudes ($A_{u_{bc}}$ and $A_{v_{bc}}$) and phases ($\phi_{u_{bc}}$ and $\phi_{v_{bc}}$) of the zonal and meridional baroclinic M_2 tidal velocities are all interpolated onto $0.1° \times 0.1°$ regular longitude–latitude grids. The interpolated amplitudes $A_{u_{bc}}$ and $A_{v_{bc}}$ are used to estimate the kinetic energy of the M_2 internal tides in section 4, since this energy is related to wave motions satisfying the dispersion relation of internal tides, as will be shown in section 5.

b. Two-dimensional wavenumber spectral analysis

A two-dimensional wavenumber spectral analysis is used to diagnose the wavelengths of the M_2 internal tide. The analysis is based on the standard two-dimensional complex discrete Fourier transform. We reconstruct the complex velocities with the in-phase and quadrature baroclinic velocities being the real and imaginary components, respectively. The in-phase and quadrature velocities are a quarter of a period apart, and are expressed, taking u_{bc} as an example, as $A_{u_{bc}}\cos\phi_{u_{bc}}$ and $A_{u_{bc}}\sin\phi_{u_{bc}}$. The spectral analysis is applied to these complex velocities in boxes of the size $15°/\cos\varphi$ (in longitude) $\times 15°$ (in latitude) with φ being the latitude. For each $15°/\cos\varphi \times 15°$ box, they are further converted to velocities on an equidistant grid (with an approximate 11-km resolution). Prior to the spectral analysis, a Tukey window is used to reduce spectral leakage, which tapers the signal at the endpoints, thereby emphasizing the data in the center of a box. For a given level, u_{bc} and v_{bc} inside a $15°/\cos\varphi \times 15°$ box are decomposed into two-dimensional plane waves with Fourier coefficients $U(k,l)$ and $V(k,l)$ as wave amplitudes, where k and l are the zonal and meridional wavenumbers, respectively. To obtain a near-global map overlapping boxes are analyzed, each shifted by $5°$. Wavenumber spectra $S_{u_{bc}}(k, l)$ and $S_{v_{bc}}(k, l)$ are then given by

$$S_{u_{bc}}(k,l) = |U(k,l)|^2, \quad \text{and} \quad (4a)$$

$$S_{v_{bc}}(k,l) = |V(k,l)|^2. \quad (4b)$$

The average of $S_{u_{bc}}(k, l)$ and $S_{v_{bc}}(k, l)$ results in the spectrum of the kinetic energy, denoted by $S_{KE}(k, l)$, in which velocities in both horizontal directions are taken into account for a robust result. The corresponding wavenumber spectra in the (k, l) wavenumber plane are then converted into $S_{KE}(K)$, which are functions of the horizontal wavenumber $K = \sqrt{k^2 + l^2}$. By moving the box horizontally, wavenumber spectra at different locations can be obtained. The horizontal wavelength is identified from the wavenumber where $S_{KE}(K)$ has a local maximum. Obviously, this diagnostic will work well when there is a distinct spectral peak, but it will produce an ambiguous result when the spectrum is flat. Note that we make no interpolations for land points inside a box. Instead, $U(k, l)$ and $V(k, l)$ are calculated from available water points in a box. Only boxes in which land points are less than 15% are considered.

Generally, stratification and the bathymetry (and consequently the water depth) vary from grid point to grid point so that different wavelengths are expected from the dispersion relation. The wavelength derived from the spectral analysis cannot capture such variations and has to be considered as an averaged wavelength within the considered box. Here, "average" does not refer to an "arithmetic mean," but rather the fact that the spectral analysis provides only one estimate of the wavelength corresponding to each local maximum from $S_{KE}(K)$ in a given box. This has to be kept in mind when comparing the wavelengths derived from wavenumber spectra of the STORMTIDE products with those obtained from the linear internal wave theory using a prescribed stratification and water depth. Wavelengths derived from the STORMTIDE model simulation will be denoted by L_{ST}.

In the present paper the goal is to estimate the wavelengths of internal tides simulated by an ocean circulation model and compare them with the wavelengths derived from the linear wave theory. Thus, a (vertical) modal decomposition of the baroclinic tidal velocities, as usually performed for point observation, is not adequate, since it would implicitly constrain the results by assumptions given by the mode computations. Thus, the horizontal spectral analysis seems to be beneficial to derive the quantity of simulated internal tide wavelengths and further, with the windowing of the velocities prior to the spectral analysis and the shifting of the boxes by 5°, a near-global map with a resolution of 5° can be obtained. To divide into mode1 and mode 2 internal tides, we will analyze the three-dimensional

fields of baroclinic tidal velocities on different model levels, as further detailed in section 5a.

It is noted that the size of the box is a compromise between the demand to obtain a more reliable estimate of the spectral peaks on the one hand and a more detailed map of the geographical variations of the wave environment on the other hand. The former requires a larger box size but the latter a smaller box size. We found a $15°/\cos\varphi \times 15°$ box size to be a reasonable compromise.

c. The Sturm–Liouville eigenvalue problem

To confirm that the dominant length scales identified using wavenumber spectra represent the wavelengths of the low-mode M_2 internal tides, the local dispersion relation of internal waves is derived by solving the Sturm–Liouville eigenvalue problem (e.g., Olbers et al. 2012) for stratification profiles that are simulated by the STORMTIDE model. We assume a flat bottom inside a $15°/\cos\varphi \times 15°$ box and no background current in this eigenvalue problem. The water depth inside a box corresponds to the box-averaged depth. Topographic features and background currents are only considered in the STORMTIDE simulation. The Sturm–Liouville eigenvalue problem is defined by

$$\frac{1}{N^2(z)} \frac{d^2}{dz^2} w_m(z) = -\nu_m w_m(z), \quad m = 1, 2, \ldots \quad (5)$$

together with boundary conditions of the flat bottom and rigid lid, in which z refers to the vertical axis, $N(z)$ is the buoyancy frequency, and $w(z)$ is the vertical structure of the waves. The vertical mode number m refers to the mth eigenvector $w_m(z)$ with the corresponding eigenvalue ν_m. The eigenvalue ν_m defines the dispersion relation,

$$\nu_m = \frac{K_m^2}{\omega^2 - f^2}, \quad (6)$$

in which ω and f are the M_2 tidal frequency and the Coriolis parameter, respectively. Given a box-averaged stratification profile, $w_m(z)$ and ν_m are obtained by numerically solving the Sturm–Liouville eigenvalue problem. The horizontal wavelength, denoted by $L_{SL,m}$ and defined as

$$L_{SL,m} = \frac{1}{K_m} = \frac{1}{\sqrt{\nu_m(\omega^2 - f^2)}}, \quad (7)$$

corresponds to the mth vertical mode. Thus, $L_{SL,m}$ is determined solely by the local stratification profile and the Coriolis parameter.

To be consistent with the wavenumber spectral analysis, we solve the Sturm–Liouville eigenvalue problem

for the same $15°/\cos\varphi \times 15°$ boxes using the box-averaged stratification and water depth. The box-averaged monthly mean temperature and salinity are used to calculate the corresponding box-averaged N. The resulting N is always well defined (i.e., real). When $N < 10^{-10}\,\text{s}^{-1}$, it is interpolated with the neighboring points in solving the eigenvalue problem. Note that the horizontal variations of stratification within each box are neglected, whereas box-averaged vertical variations are taken into account. The stratification available on the model levels is then interpolated onto a vertical grid with a resolution of 10 m that is used to numerically solve the eigenvalue problem.

Since the Sturm–Liouville eigenvalue problem is derived from the linear internal wave theory, the question of whether the STORMTIDE model is capable of simulating internal tides is answered by a comparison of the wavelengths obtained from the Sturm–Liouville eigenvalue problem with those obtained by applying spectral analysis to the STORMTIDE simulation.

4. Kinetic energy of the M$_2$ internal tide

Since it is difficult to diagnose the kinetic energy related to internal tides from the observations, we present here a quantification of this energy based on the STORMTIDE simulation. Figures 2a and 2b show the horizontal distributions of the kinetic energy of the M$_2$ internal tide at 100 and 1085 m, respectively. As will be discussed in section 5a, 100 and 1085 m are depths at which two different modes dominate, respectively. The kinetic energy at 100 m is much stronger than that at 1085 m. The overall structures resemble those of the satellite-observed internal tide surface signatures, and are characterized by hot spots at both depths, for example, near Madagascar, Hawaii, east of the Philippines, and the tropical South and southwest Pacific. The maxima of the kinetic energy correspond to a current speed of about 5–6.5 cm s^{-1} at 100 m and 1.5–2 cm s^{-1} at 1085 m for the M$_2$ internal tide. For comparison, the typical speed of maximum transient eddying currents is about 30 cm s^{-1} at 100 m (von Storch et al. 2012). The globally integrated kinetic energy of the M$_2$ internal tide is about 0.08 EJ (1 EJ = 10^{18} J). This is about 20% of the internal wave energy (von Storch et al. 2012) that results presumably from wind-induced near-inertial waves.

Figure 2c shows the vertical integral of the kinetic energy with a spatial pattern comparable to those at 100 and 1085 m. The amplitude and the structure compare also well with the M$_2$ internal tide energy obtained by solving two coupled equations describing integrated versions of the radiative transfer equations for the M$_2$ internal tide and a wave continuum (Eden and Olbers 2014, their Fig. 5b). One of the main differences is the beamlike structures that are absent in the figure by Eden and Olbers (2014). This difference results from the fact that Eden and Olbers (2014) assumed for simplicity a uniform distribution of the wave propagation angle in the forcing term. Consequently, the equations considered do not distinguish waves with different wavevector angles. If the wave sources are not homogeneously distributed, then waves propagating from the individual generation sites, characterized by beamlike structures, would stand out more clearly, as in case of Fig. 2c.

5. Wavelengths of the model-simulated M$_2$ internal tide

### a. Characteristics of wavenumber spectra

Before considering the wavelengths, we first study the characteristics of the two-dimensional wavenumber spectra. Figure 3 shows spectra $S_{KE}(k, l)$ in the left column, with both positive and negative wavenumbers (Figs. 3a and 3c), at both 100 and 1085 m in the $15°/\cos\varphi \times 15°$ box centered at 22.55°N, 170°W. At 100 m (Fig. 3a), a distinct spectral peak of $S_{KE}(k, l)$ is shown in the form of a near-circle band on the (k, l) plane. This most energetic band is located within the range of K of about 0.005–0.01 km^{-1}, corresponding to a horizontal wavelength of 100–200 km. A less pronounced band is located at relatively larger wavenumbers, with K being around 0.015 km^{-1}, corresponding to a wavelength of about 65 km. In the ocean's interior at 1085 m, two spectral peaks are also located at the same wavenumber bands. In contrast to the spectrum at 100 m, the high-wavenumber peak, with a broader bandwidth, is stronger than the low-wavenumber peak. Some spectral energy much weaker than the two spectral peaks is also found at still higher wavenumbers at both depths.

The two spectral peaks remain well defined when converting $S_{KE}(k, l)$ into $S_{KE}(K)$ in Figs. 3b and 3d. The blue dots show $S_{KE}(K)$ obtained from each wavenumber vector (k, l). The red lines represent the bin averages of $S_{KE}(K)$ that are averaged over all values of $S_{KE}(K)$ with K inside the respective intervals. For each wavenumber, the variability indicated by the blue dots results from variations of $S_{KE}(k, l)$ along a circle centered at the origin of the (k, l) plane. These variations indicate properties of wave propagation. For waves generated at a few selected source sites, maxima of the respective two-dimensional wavenumber spectra will not have the same strength in all directions. For instance, in Fig. 3a, the low-wavenumber peak has the largest values in the southwest and northeast directions. Thus, waves associated with the low-wavenumber peak in the box considered in Fig. 3 propagate preferably along a line orientated in the southwest–northeast direction.

(a) Kinetic energy, 100 m
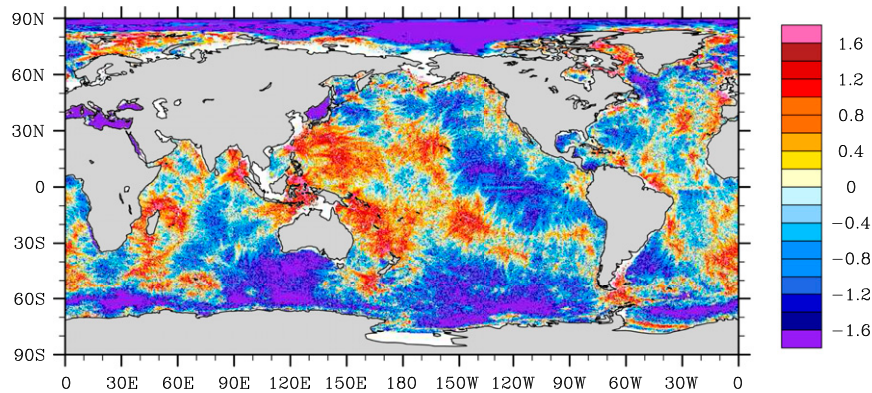
(b) Kinetic energy, 1085 m
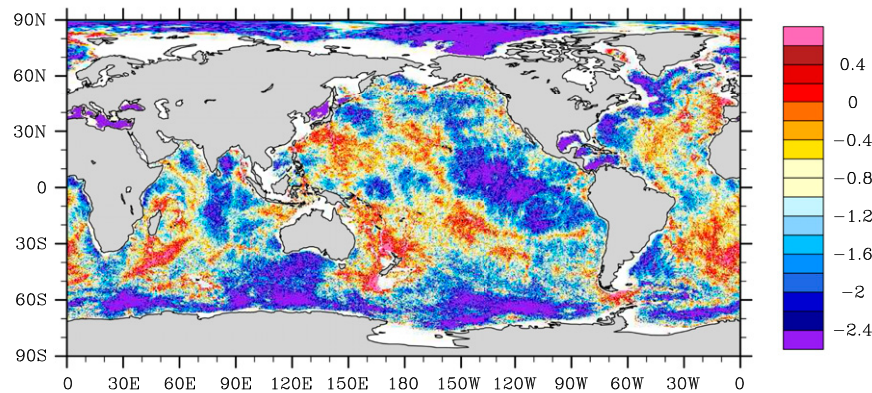
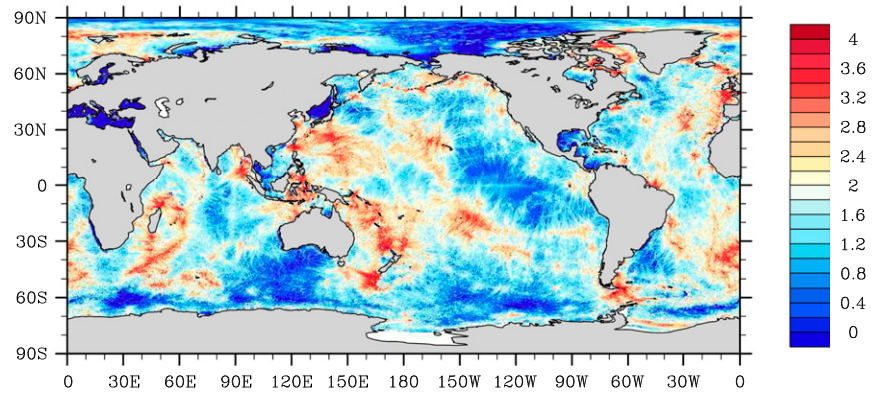(c) Vertical integral of the kinetic energy

FIG. 2. Kinetic energy $(cm^2 s^{-2})$ of the M_2 internal tide in logarithmic scales at (a) 100 and (b) 1085 m. (c) The vertical integral of the kinetic energy $(J\,m^{-2})$ in logarithmic scales , which is prepared in the same scales as used in Eden and Olbers (2014, their Fig. 5b). The kinetic energy at a single depth is derived using $(A_{u_{bc}}^2 + A_{v_{bc}}^2)/2$, with $A_{u_{bc}}$ and $A_{v_{bc}}$ being amplitudes of the M_2 baroclinic zonal and meridional velocities, respectively. The vertical integral is then derived by $\int_{-H}^{0} \rho_w (A_{u_{bc}}^2 + A_{v_{bc}}^2)/2\,dz$, with ρ_w being the density of seawater.

(a) $\log(S_{KE}(k,l))$ at 100 m

(b) $S_{KE}(K)$ at 100 m

(c) $\log(S_{KE}(k,l))$ at 1085 m

(d) $S_{KE}(K)$ at 1085 m
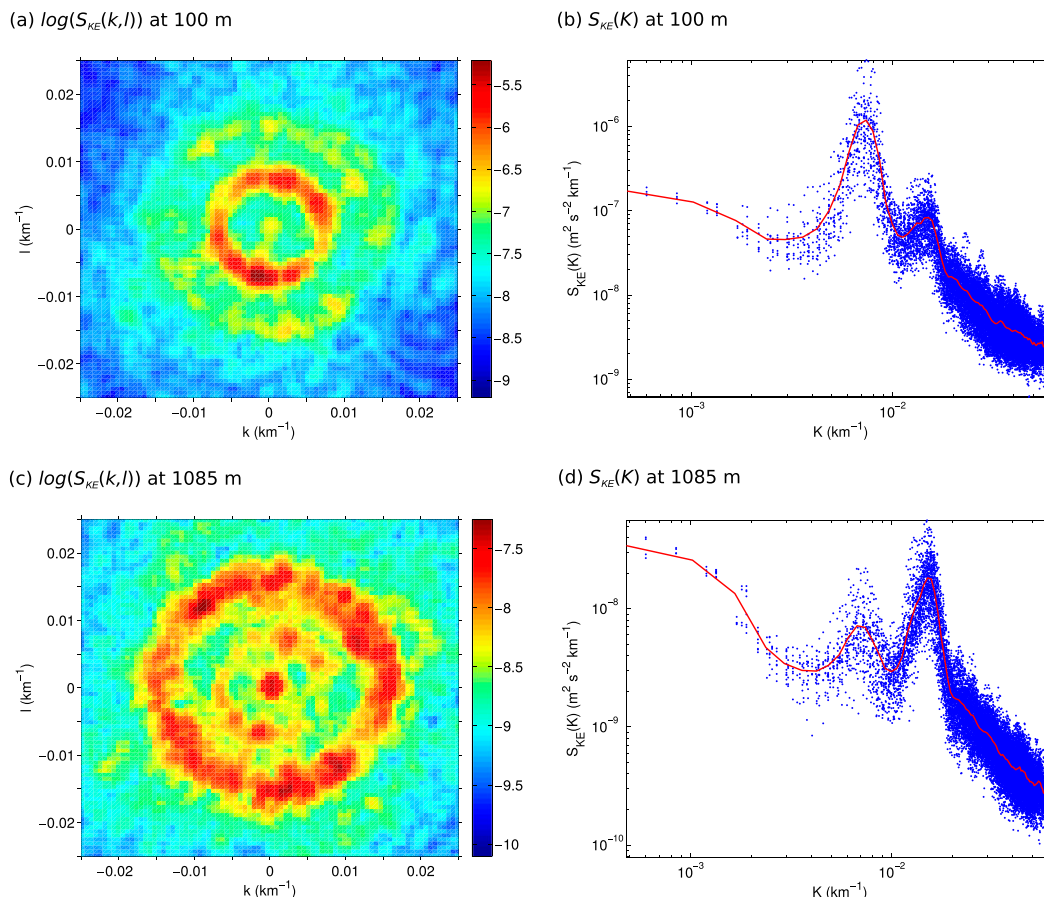
FIG. 3. Wavenumber spectra $S_{KE}(k, l)$ of the kinetic energy of the M_2 internal tide at (a) 100 and (c) 1085 m in logarithmic scales in the $15°/\cos\varphi \times 15°$ box centered at (22.55°N, 170°W). The resolved range of the zonal and meridional wavenumbers is within -0.045–0.044 km^{-1}. To enhance the readability, we show only the range of -0.025–0.025 km^{-1} that involves the most energetic motions and leave out wavenumber regions with very weak energy. In the right column, wavenumber spectra $S_{KE}(K)$ of the M_2 internal tide are shown at (b) 100 and (d) 1085 m, converted from $S_{KE}(k, l)$ using $K = \sqrt{k^2 + l^2}$ in the same box. The scattered blue dots are converted directly from each value of $S_{KE}(k, l)$. The red lines represent the bin averages of $S_{KE}(K)$, in which $S_{KE}(K_i)$ at the ith interval is obtained by averaging all values of $S_{KE}(K)$ with K inside the interval $(K_i, K_i + \Delta)$. We consider a total of 100 consecutive intervals. Term Δ is obtained by dividing the total resolved wavenumber range by 100.

We now consider the vertical dependence of $S_{KE}(K)$ in terms of the example shown in Fig. 4. Overall, the spectral energy decreases with increasing depth. The low-wavenumber peak is strongest in the upper ocean, followed by a reduction until the energy drops to a minimum at 1220 m (red dotted line). The spectral peak reemerges farther downward. The high-wavenumber spectral energy undergoes more complicated variations. The spectral peak is detectable in the top 100 m and diminishes downward, and disappears to different degrees in the depth range 122–485 m. It becomes evident again farther below and clearly stand out in the depth range 560–1700 m. Below 1700 m, it is strongly weakened.

To understand the depth dependence of the low- and high-wavenumber peaks of $S_{KE}(K)$, we introduce the vertical modal structures of the kinetic energy of modes

1 and 2 (the right panel of Fig. 4b). These vertical structures are derived by solving the Sturm–Liouville eigenvalue problem [see Eq. (5), for $m = 1$ and 2] using the box-averaged stratification profile shown in the left panel of Fig. 4b. They show a zero crossing at around 1220 m for mode 1 and an interior maximum at about 750 m between two zero crossings at about 350 and 2200 m for mode 2. The variations with depth of both low- and high-wavenumber spectral peaks shown in Fig. 4a correspond, in general, to the vertical structures of the first two modes of the Sturm–Liouville eigenvalue problem. In particular, we observe a loss of the low-wavenumber peak and find only the high-wavenumber peak at 1220 m. This is consistent with the fact that the amplitude of mode 1 undergoes its zero crossing at this depth, while the amplitude of mode 2 remains strong.

(a) $S_{KE}(K)$
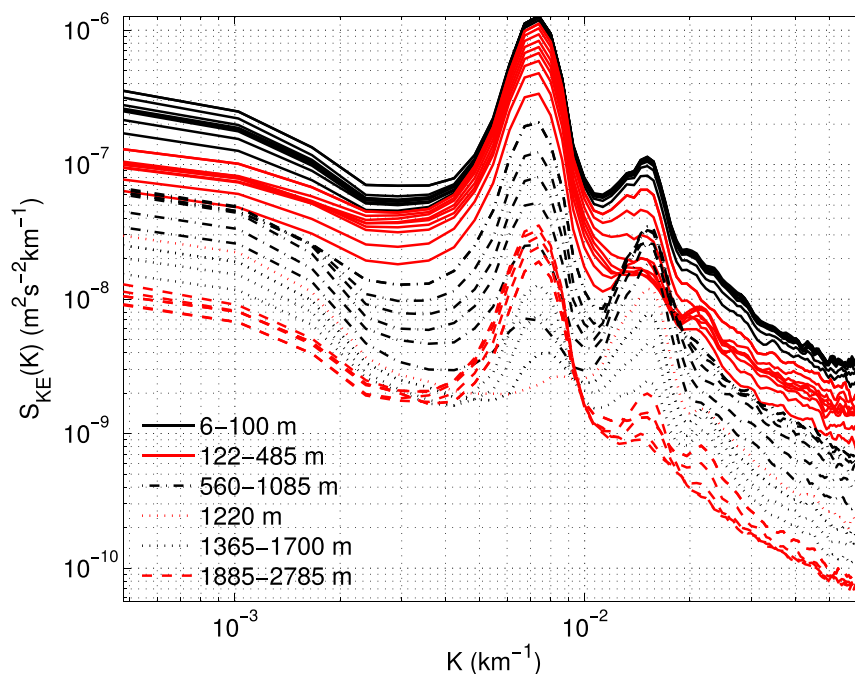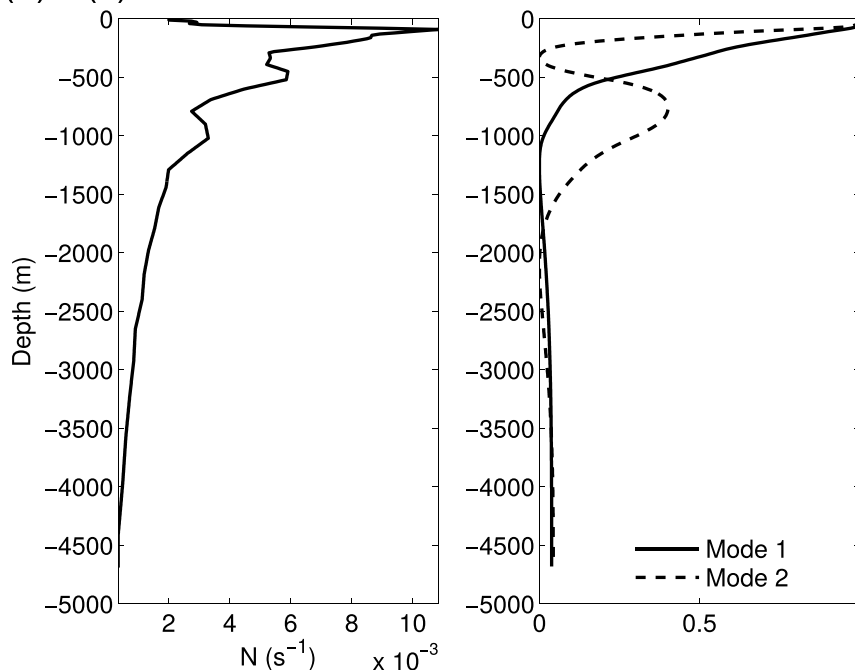

(b) $N(z)$ and modal structures

FIG. 4. (a) Bin-averaged spectra $S_{KE}(K)$ of the horizontal kinetic energy of the M_2 internal tide derived for the 15°/cos$\varphi \times$ 15° box centered at (22.55°N, 170°W). (b) Shown are (right) the vertical modal structures of mode 1 (solid) and mode 2 (dashed) of the kinetic energy in the considered box, which are proportional to $[dw_m(z)/dz]^2$ with $w_m(z)$ being the eigenfunction of Eq. (5). These structures are derived by solving the Sturm–Liouville eigenvalue problem with (left) the box-averaged stratification profile simulated by the STORMTIDE model.
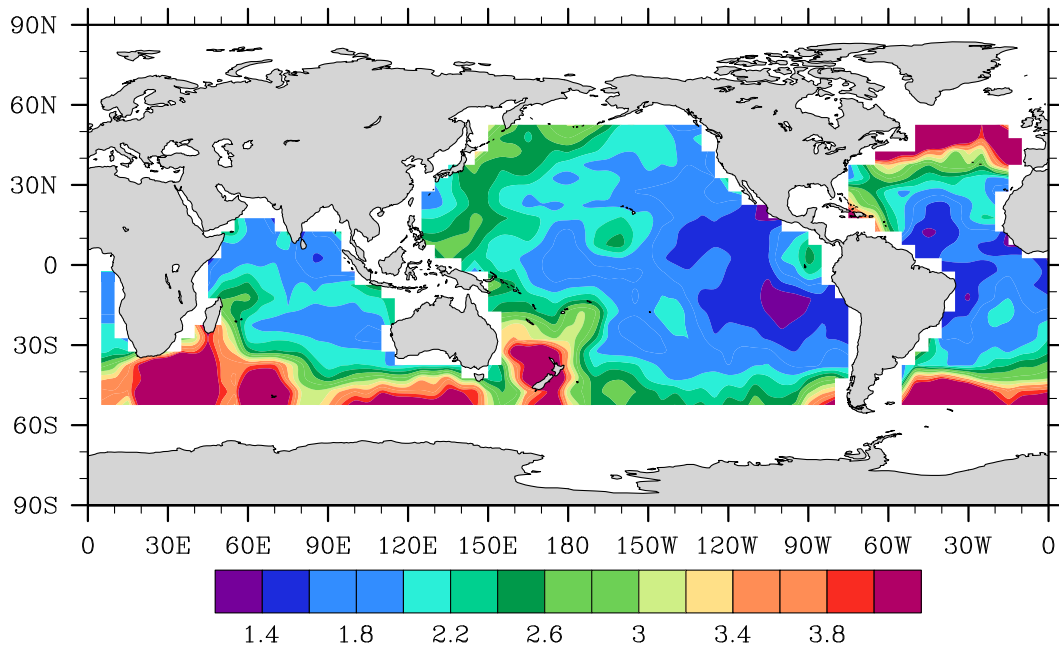
FIG. 5. Normalized spectral width ($\times 10$) derived from the mode 1 wavenumber spectra. The width is defined by the wavenumber interval between half of the peak energy, and is then normalized by the wavenumber related to the spectral peak. Nine-point smoothing has been performed after deriving the raw near-global map.

Hence, the low- and high-wavenumber peaks are proved to be actually modes 1 and 2, respectively.

As for the box considered in Fig. 4a, both mode 1 and mode 2 have the same wavenumber throughout the water column in all considered boxes. This result reflects the fact that the horizontal wavelength of a mode is independent of depth, indicating that certain layers with energetic internal tides can be selected to efficiently identify the wavenumbers of each mode. For this purpose, we have examined the zero-crossing depths of modes 1 and 2. The mode 1 zero crossings, in regions with less than 15% land points—that is, in the open ocean—are located at depths deeper than 700 m. Mode 2 undergoes its first zero crossings at levels shallower than 900 m, while its second zero crossing is located at depths deeper than 1400 m, both in the open ocean. Thus, performing spectral analysis on velocities at 100 and around 1000 m, which depart from the depths of the zero crossings of modes 1 and 2, respectively, one should be able to identify the wavelengths of modes 1 and 2. In the following, the near-global map of the mode 1 wavelengths $L_{ST,1}$ is hence derived from $S_{KE}(K)$ at 100 m in section 5b. In the deeper ocean (e.g., around 1000 m), mode 2 is energetic, while mode 1 possesses normally only weak energy. Hence, the near-global map of the mode 2 wavelengths $L_{ST,2}$ is derived from $S_{KE}(K)$ at 1085 m.

In the process of performing spectral analysis for the kinetic energy of internal tides in boxes covering the near-global ocean, we realize that the spectral peaks are difficult to detect in regions with strong mesoscale eddies. The normalized spectral width of mode 1 is shown in Fig. 5. We can see that larger spectral widths mainly occur in strong current regions, for instance, the Kuroshio and the Gulf Stream as well as their extensions, and the Antarctic Circumpolar Current regions in the southern high latitudes. In these regions, the peaks are broadened. When the peaks get too broad or even turn to flat spectra, identification of the associated wavenumber will be hardly possible. Thus, we neglect the regions poleward of 52.55°N/52.45°S in the following near-global analysis.

b. Geographical distribution of wavelengths

The map of $L_{ST,1}$ (Fig. 6a) shows that the scales of mode 1 are around 100–160 km in most regions, with the wavelengths shorter than 100 km existing only in the very eastern equatorial region in the Pacific, in the southern Indian Ocean, and in the eastern equatorial Atlantic. The wavelengths longer than 170 km emerge mainly in the mid- and high latitudes, for instance, east of Japan and in the southwestern Pacific and south of Australia. This distribution reflects both a general poleward increase in $L_{ST,1}$ and a zonal asymmetry that is more pronounced in the Pacific than in the other two ocean basins.

The mode 2 wavelengths (Fig. 7a) are around 45–80 km. The $L_{ST,2}$ in the Atlantic are generally in the
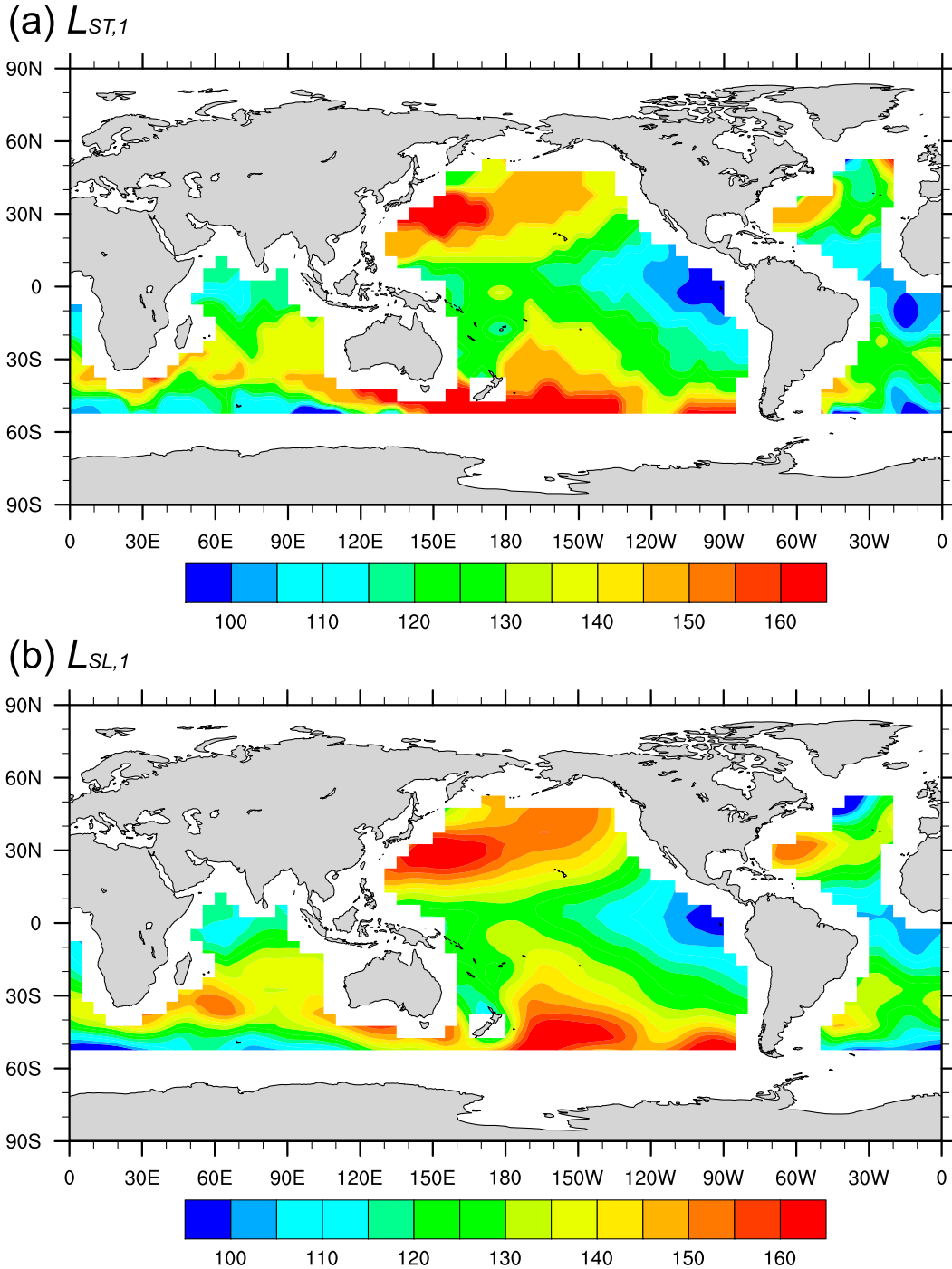
(a) $L_{ST,1}$

(b) $L_{SL,1}$

FIG. 6. Distributions of the mode 1 wavelengths (km) for the M_2 internal tide as derived (a) by applying two-dimensional wavenumber spectral analysis to the M_2 baroclinic velocities at 100 m simulated by the STORMTIDE model for overlapping $15°/\cos\varphi \times 15°$ boxes, and (b) by numerically solving the Sturm–Liouville eigenvalue problem. The eigenvalue problem uses the stratification profiles averaged over the same boxes as used in the spectral analysis.

range of 45–65 km and have the lowest values among the three ocean basins. The length scales of mode 2 in the Indian Ocean are around 50–80 km, with the longest wavelengths appearing in the

northeastern part. Waves in the Pacific show a clear zonal asymmetry with wavelengths longer than 75 km mainly in the northwestern Pacific and in the western tropical Pacific, and with wavelengths
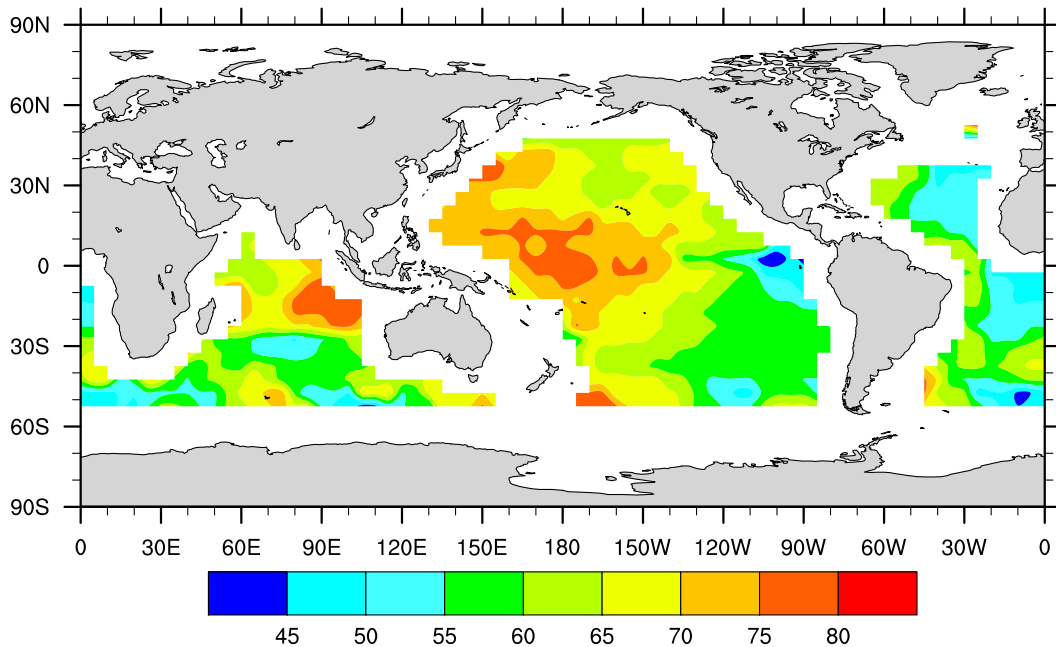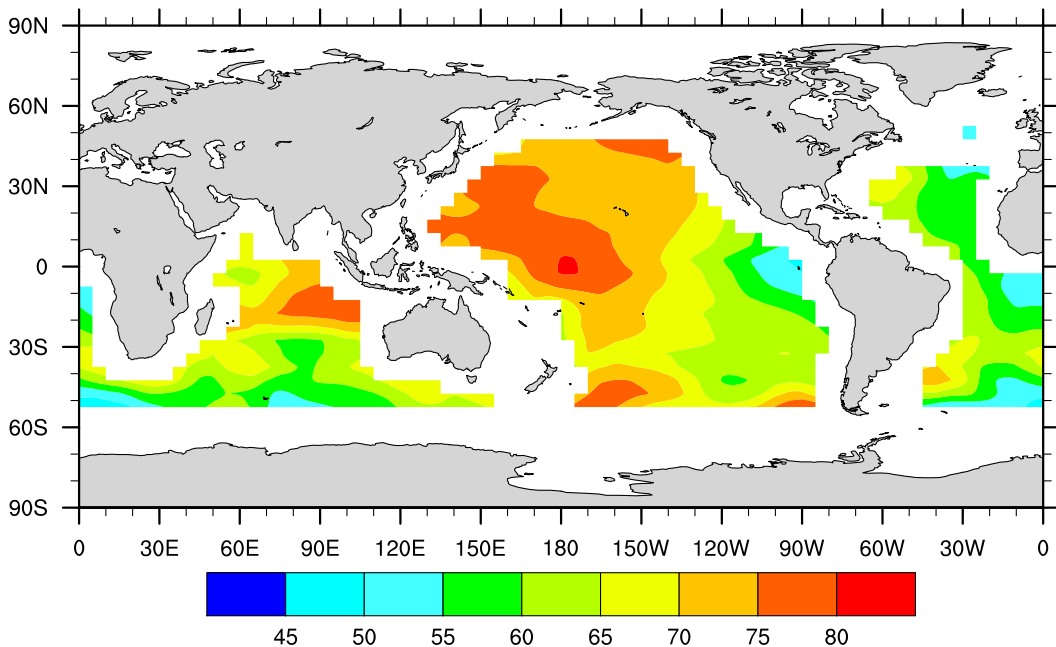
(a) $L_{ST,2}$

(b) $L_{SL,2}$

FIG. 7. Distributions of the mode 2 wavelengths (km) for the M_2 internal tide. The same methods are used as in Fig. 6, except that the spectral analysis is performed for the STORMTIDE M_2 baroclinic velocities at 1085 m for deriving $L_{ST,2}$.

shorter than 60 km in the southeastern South Pacific. The mode 2 wavelengths reveal a strong zonal asymmetry that outweighs the meridional variation and is much more pronounced than the zonal asymmetry of $L_{ST,1}$.

c. Comparison with the distribution obtained by solving the eigenvalue problem

The geographical distribution of $L_{ST,1}$ is comparable with that of $L_{SL,1}$. Figure 8a shows that the

(a) $(L_{ST,1}-L_{SL,1})\times 100/L_{ST,1}$

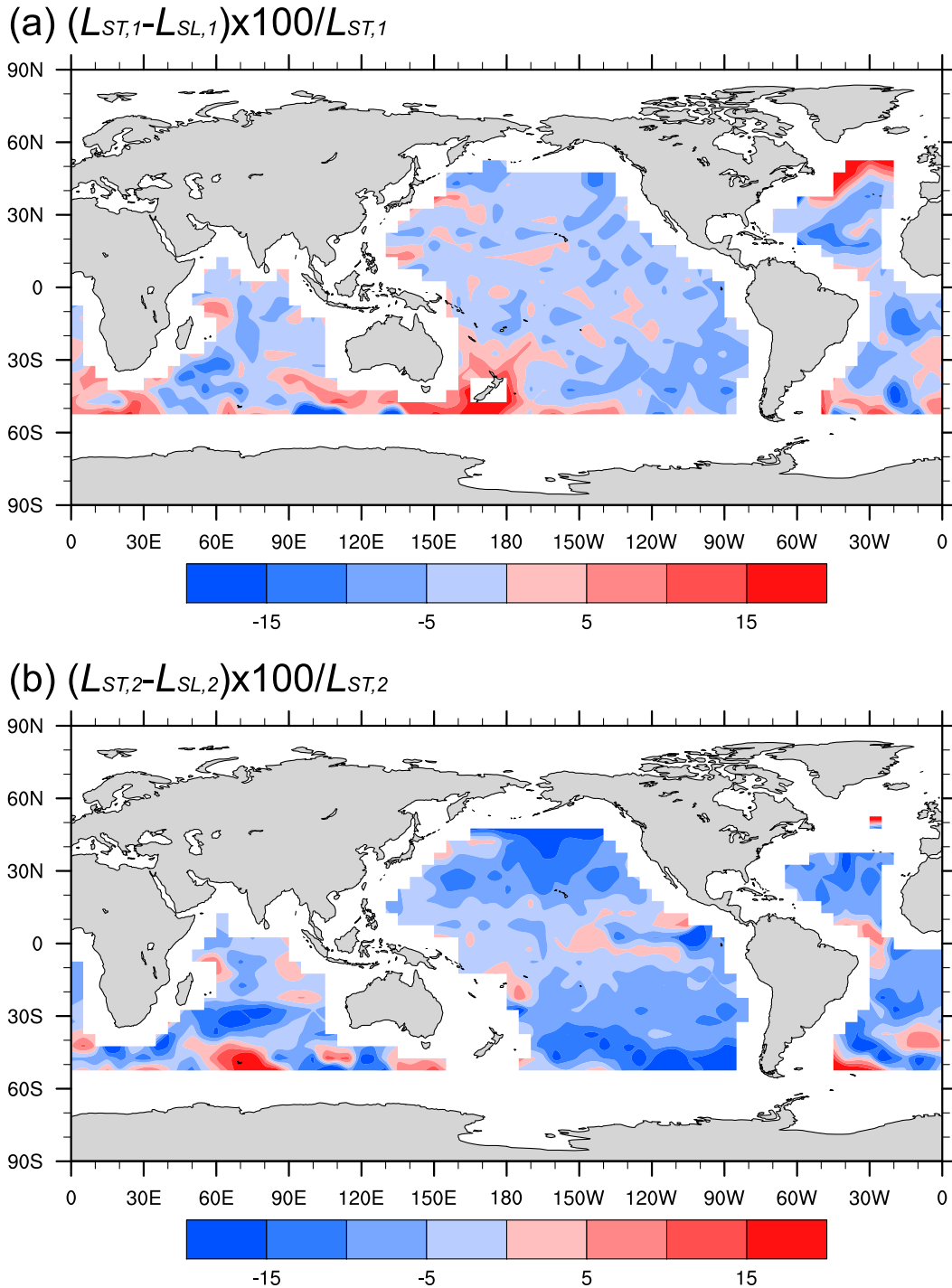## (b) $(L_{ST,2}-L_{SL,2})\times 100/L_{ST,2}$

FIG. 8. Differences (%) between $L_{ST,m}$ and $L_{SL,m}$ ($m = 1, 2$) for (a) mode 1 and (b) mode 2 normalized by values of $L_{ST,m}$. Red shading indicate that the values of $L_{ST,m}$ are larger than those of $L_{SL,m}$, whereas blue shading suggest the opposite.

relative differences are primarily under 10% of the local wavelengths in around 90.6% of the global ocean considered, and under 5% of the local wavelengths in two-thirds of the global ocean. The small

differences lead to good agreement between the zonal-mean $L_{ST,1}$ and $L_{SL,1}$ in Fig. 9a. In high latitudes, mainly in the Indian Ocean and Atlantic, larger discrepancies also arise, but with only 3% of the

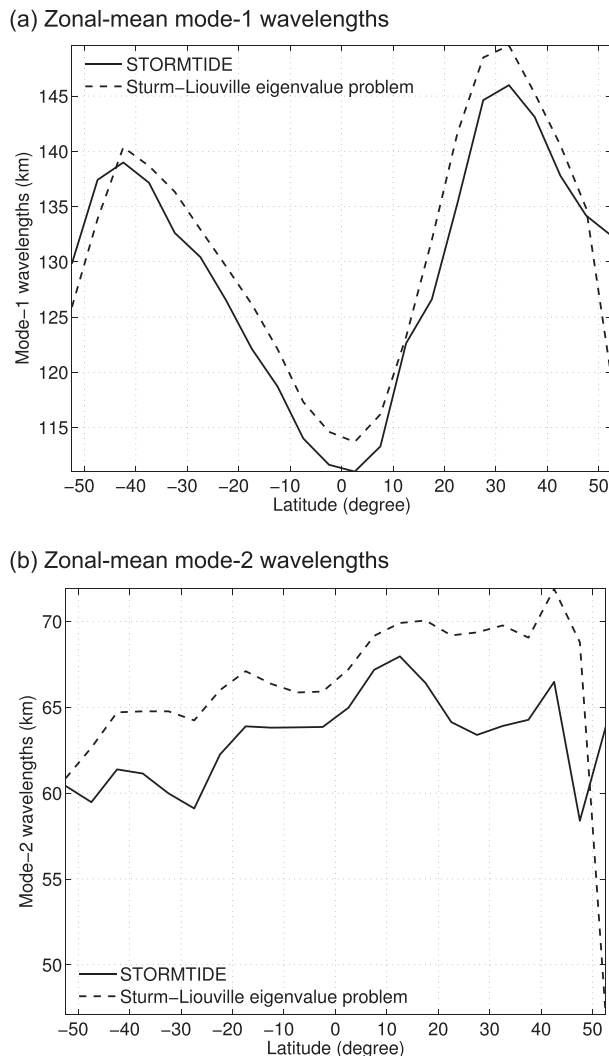(a) Zonal-mean mode-1 wavelengths

(b) Zonal-mean mode-2 wavelengths

FIG. 9. Zonal-mean wavelengths of (a) mode 1 and (b) mode 2. The solid line represents $L_{ST,m}$, which is obtained from the STORMTIDE simulation, and the dashed line represents $L_{SL,m}$, which is derived by solving the Sturm–Liouville eigenvalue problem.

mainly in high latitudes. With respect to zonal means, the meridional profile of $L_{ST,2}$ is comparable with that of $L_{SL,2}$ (Fig. 9b). Overall, mode 2 shows larger relative discrepancies than mode 1, which makes sense since shorter waves are more easily affected by the varying oceanic medium, introducing a stronger nonlinear effect.
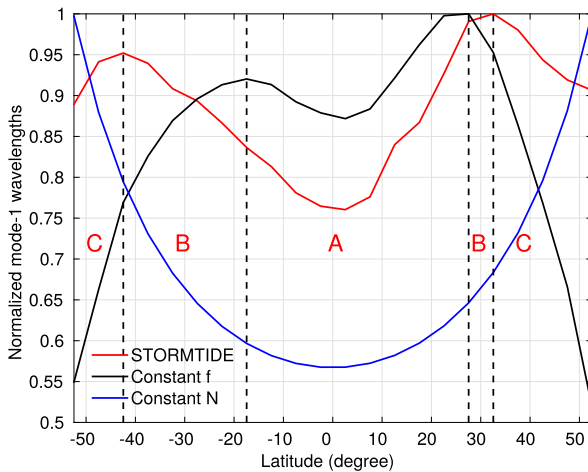
6. Relative roles of N and f in determining the wavelengths

The mode 1 wavelengths simulated by the STORMTIDE model (Fig. 6a) reveal a zonal asymmetry and a general poleward increase. The same features are observed in the results of the Sturm–Liouville eigenvalue problem (Fig. 6b), whose solutions solely depend on the local stratification N and on the Coriolis parameter f. We now explore the relative roles of N and f in determining the distribution of the wavelengths. Along a latitude circle, since f is constant, the zonal asymmetry must result from the effect of N.

To further separate the roles of N and f in determining the wavelengths, we design another two near-global maps of the mode 1 wavelengths using the linear theory. One is derived by using constant f in Eq. (7) with the eigenvalues directly from the eigensolutions [Eq. (5)], whereas the other is acquired by setting constant stratification, hence constant ν_m in Eq. (7), in the near-global ocean in which f varies realistically with latitudes. Their normalized zonal-mean values, shown in Fig. 10a, are independent of the values of N and f that have been chosen. We find a poleward increase of the wavelengths with constant stratification (blue line), a tendency introduced by the dependence of f on latitudes. The wavelengths will further proceed infinity at the critical latitude of about 74.5°N/S, where f approaches the M_2 tidal frequency. The wavelengths determined by N only (black line) decrease equatorward in the low latitudes between 28°N and 18°S, and decrease poleward beyond this latitude range, a feature introduced by the variations of ν_m with latitudes.

The normalized zonal-mean $L_{ST,1}$ is also displayed in Fig. 10a (red line). Between 28°N and 18°S (region A in Fig. 10a), the $L_{ST,1}$ goes up sharper than both theoretical wavelengths, indicating the combined positive contributions from both N and f in determining the wavelengths. In the latitudes between 28° and 33°N and 18° and 42°S (region B), the $L_{ST,1}$ continues rising although N imposes here a negative contribution to the wavelengths. Hence, in these two regions, the role of f dominates over that of N. However, poleward beyond 42°S/33°N (region C), the role of N outweighs that of f as a result of a poleward decrease of $L_{ST,1}$. This explains

global ocean considered having a relative difference larger than 15%. The result indicates that in most of the global ocean, particularly in the Pacific, the mode 1 M_2 internal tide simulated by the STORMTIDE model is well explained by linear waves that satisfy the local dispersion relation, diagnosed locally, with other effects accounting for less than 10% in terms of relative differences.

Figure 8b shows mainly negative relative discrepancies of mode 2, indicating that the simulated mode 2 wavelengths are in general shorter than those predicted by the Sturm–Liouville eigenvalue problem. The relative differences are under 10% in about 73% of the global ocean considered. Larger discrepancies occur

(a) Normalized mode-1 wavelengths

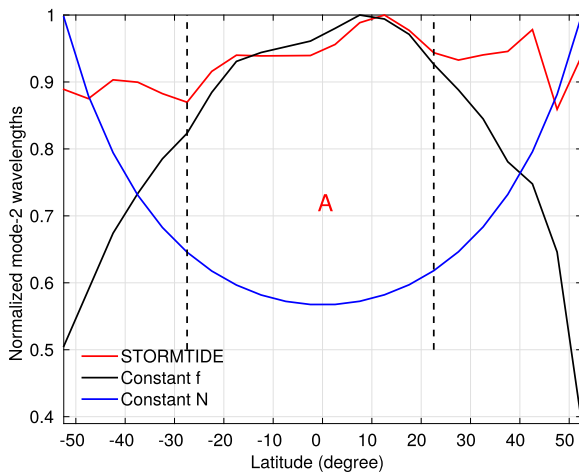(b) Normalized mode-2 wavelengths

FIG. 10. Zonal-mean wavelengths of (a) mode 1 and (b) mode 2 derived by the spectral analysis with the simulated M_2 baroclinic velocities (red); by setting constant N, hence constant ν_m in Eq. (7) (blue); and by setting constant f in Eq. (7) by ν_m directly from solving the eigenvalue problem Eq. (5) (black). These wavelengths are normalized by their respective maximum. The latitude space is further divided into characteristic regions, denoted by A–C for mode 1 and denoted by A for mode 2, which are further described in the text.

the differences of our results, specifically for high latitudes, to that of a two-layer model with a horizontally uniform stratification but a latitudinal dependence of f in Simmons et al. (2004a, their Fig. 11). Hence, we conclude that N and f play a combined role in determining the geographical distribution of $L_{ST,1}$.

For the mode 2 wavelengths (Fig. 7a), we find that the tendency of a poleward increase in wavelengths almost no longer exists and even reverses in the southern Atlantic and part of the Indian Ocean. Hence, the role of f is significantly weakened in determining $L_{ST,2}$

compared to its role in determining $L_{ST,1}$, consistent with the fact derived from Eq. (7) that the same amount of changes in f will lead to smaller changes in mode 2 than in mode 1 as a result of the larger eigenvalues of mode 2. The zonal asymmetry on the other hand is more pronounced for $L_{ST,2}$ than for $L_{ST,1}$, in particular in the Pacific. This feature is also captured in $L_{SL,2}$ (Fig. 7b). It seems that stratification has a stronger influence on $L_{ST,2}$ than on $L_{ST,1}$, consistent with the description that higher modes are more sensitive to the ocean environment (Ray and Zaron 2011), and thus controls the global characteristics of $L_{ST,2}$.

The normalized zonal mean of the simulated mode 2 wavelengths are shown in Fig. 10b in comparison with those derived with either N or f fixed. The simulated mode 2 wavelengths (red line) are generally well captured by those derived with constant f (black line) between about 28°S and 23°N (region A in Fig. 10b), and they depart outside this latitude range. There is only a slight increasing tendency of $L_{ST,2}$ with increasing latitudes. Hence, f seems not to play a significant role in determining mode 2 wavelengths. In conclusion, the effect of N outweighs that of f in determining the simulated mode 2 wavelengths.

7. Concluding remarks

With a spectral analysis of the near-global three-dimensional field of model-simulated baroclinic tidal velocities, we examined the horizontal wavelength properties of mode 1 and mode 2 internal tides. The model is a $1/10°$ primitive equation model that concurrently simulates the ocean circulation and tides. The near-global distributions of the simulated internal tide wavelengths are compared to those obtained by solving the Sturm–Liouville eigenvalue problem. The analysis aims not only to identify the wavelengths of the low-mode M_2 internal tides and their large-scale characteristics but also to quantify various factors that affect the wavelengths and hence the M_2 internal tide. The following conclusions are drawn.

1) Two modes of the M_2 internal tide are captured by the STORMTIDE model. The mode 1 wavelengths ($L_{ST,1}$) are in the range of 100–160 km. The largest values are above 170 km and exist in strong current regions, for instance, in the Kuroshio and Antarctic Circumpolar Current regions. The geographical distribution reveals a zonal asymmetry and a general tendency of increasing $L_{ST,1}$ with increasing latitude. The model-simulated internal tide mode 2 wavelengths ($L_{ST,2}$) are primarily in the range of 45–80 km. Values larger than 75 km are mainly concentrated in the

equatorial regions of the Pacific and in the northeast region of the Indian Ocean. The dominant feature of $L_{ST,2}$ is the zonal asymmetry, whereas the latitudinal variations are not as pronounced as that of $L_{ST,1}$. This characteristic is explained by the dispersion relation derived directly from the Sturm–Liouville eigenvalue problem, which depends primarily on the local stratification N and the Coriolis parameter f. Obviously, the zonal asymmetry of the wavelengths is a result of variation in N only, whereas the meridional variations are caused by a combination of changes in N and f. Our analysis shows that for the mode 1 internal tide, the wavelengths are controlled by both N and f. Instead, for the mode 2 internal tide, the variations of N dominate their spatial characteristics.

2) The STORMTIDE model simulated, to a first approximation, mainly linear internal waves that satisfy the local dispersion relation. The small differences between $L_{ST,1}$ and $L_{SL,1}$ are systematic, with $L_{ST,1}$ being smaller than $L_{SL,1}$ over most of the near-global regions. In high latitudes, larger differences between $L_{ST,m}$ and $L_{SL,m}$ are observed, suggesting the important role of nonlinear wave–current interactions there.

In general, we find that the spectral peaks are broadened considerably in eddy-active regions, for instance, within the Antarctic Circumpolar Current region. Interactions between mean flows, mesoscale eddies, and internal waves might play a role in determining the wavelengths in these regions. The broadening of the peaks could be a sign of current-induced frequency shifts (Kunze 1985), and thus it implies that frequencies of internal waves are shifted toward or away from the M_2 tidal frequency. With strong frequency shifts, the center of the peaks could also be shifted toward different wavenumbers.

In general we conclude from this study that the characteristics of internal tides are well described by the global model approach and are consistent with linear waves obtained by solving the local Sturm–Liouville eigenvalue problem. Deviations from linear waves lead to wavelength differences of about 5%–10%. Since these interactions are nonstationary processes, it will be important to further understand these complex mechanisms in order to accurately map the time-dependent characteristics for an advanced processing of future high-resolution satellite altimeter data.

REFERENCES

Arbic, B. K., A. J. Wallcraft, and E. J. Metzger, 2010: Concurrent simulation of the eddying general circulation and tides in a global ocean model. *Ocean Modell.*, **32**, 175–187, doi:10.1016/j.ocemod.2010.01.007.

——, J. G. Richman, J. F. Shriver, P. G. Timko, E. J. Metzger, and A. J. Wallcraft, 2012: Global modeling of internal tides within an eddying ocean general circulation model. *Oceanography*, **25**, 20–29, doi:10.5670/oceanog.2012.38.

Cherniawsky, J. Y., M. G. G. Foreman, W. R. Crawford, and R. F. Henry, 2001: Ocean tides from TOPEX/Poseidon sea level data. *J. Atmos. Oceanic Technol.*, **18**, 649–664, doi:10.1175/1520-0426(2001)018<0649:OTFTPS>2.0.CO;2.

Eden, C., and D. Olbers, 2014: An energy compartment model for propagation, nonlinear interaction, and dissipation of internal gravity waves. *J. Phys. Oceanogr.*, **44**, 2093–2106, doi:10.1175/JPO-D-13-0224.1.

Egbert, G. D., and R. D. Ray, 2000: Significant dissipation of tidal energy in the deep ocean inferred from satellite altimeter data. *Nature*, **405**, 775–778, doi:10.1038/35015531.

Exarchou, E., J.-S. von Storch, and J. H. Jungclaus, 2014: Sensitivity of transient climate change to tidal mixing: Southern Ocean heat uptake in climate change experiments performed with ECHAM5/MPIOM. *Climate Dyn.*, **42**, 1755–1773, doi:10.1007/s00382-013-1776-y.

Foreman, M. G. G., J. Y. Cherniawsky, and V. A. Ballantyne, 2009: Versatile harmonic tidal analysis: Improvements and applications. *J. Atmos. Oceanic Technol.*, **26**, 806–817, doi:10.1175/2008JTECHO615.1.

Green, J. A. M., and J. Nycander, 2013: A comparison of tidal conversion parameterizations for tidal models. *J. Phys. Oceanogr.*, **43**, 104–119, doi:10.1175/JPO-D-12-023.1.

Jungclaus, J. H., and Coauthors, 2006: Ocean circulation and tropical variability in the coupled model ECHAM5/MPI-OM. *J. Climate*, **19**, 3952–3972, doi:10.1175/JCLI3827.1.

Kunze, E., 1985: Near-inertial wave propagation in geostrophic shear. *J. Phys. Oceanogr.*, **15**, 544–565, doi:10.1175/1520-0485(1985)015<0544:NIWPIG>2.0.CO;2.

Maltrud, M. E., and J. L. McClean, 2005: An eddy resolving global 1/10° ocean simulation. *Ocean Modell.*, **8**, 31–54, doi:10.1016/j.ocemod.2003.12.001.

Marsland, S. J., H. Haak, J. H. Jungclaus, M. Latif, and F. Röske, 2003: The Max-Planck-Institute global ocean/sea ice model with orthogonal curvilinear coordinates. *Ocean Modell.*, **5**, 91–127, doi:10.1016/S1463-5003(02)00015-X.

Masumoto, Y., and Coauthors, 2004: A fifty-year eddy-resolving simulation of the world ocean: Preliminary outcomes of OFES (OGCM for the Earth Simulator). *J. Earth Simul.*, **1**, 35–56.

Melet, A., R. Hallberg, S. Legg, and K. Polzin, 2013: Sensitivity of the ocean state to the vertical distribution of internal-tide-driven mixing. *J. Phys. Oceanogr.*, **43**, 602–615, doi:10.1175/JPO-D-12-055.1.

Montenegro, A., M. Eby, A. J. Weaver, and S. R. Jayne, 2007: Response of a climate model to tidal mixing parameterization under present day and last glacial maximum conditions. *Ocean Modell.*, **19**, 125–137, doi:10.1016/j.ocemod.2007.06.009.

Müller, M., 2012: High resolution ocean circulation and tides. German Climate Computing Center (DKRZ), accessed 22

October 2012. [Available online at http://cera-www.dkrz.de/WDCC/ui/Entry.jsp?acronym=DKRZ_lta_510.]

——, 2013: On the space- and time-dependence of barotropic-to-baroclinic tidal energy conversion. *Ocean Modell.*, **72**, 242–252, doi:10.1016/j.ocemod.2013.09.007.

——, H. Haak, J. H. Jungclaus, J. Sündermann, and M. Thomas, 2010: The effect of ocean tides on a climate model simulation. *Ocean Modell.*, **35**, 304–313, doi:10.1016/j.ocemod.2010.09.001.

——, J. Y. Cherniawsky, M. G. G. Foreman, and J.-S. von Storch, 2012: Global M_2 internal tide and its seasonal variability from high resolution ocean circulation and tide modeling. *Geophys. Res. Lett.*, **39**, L19607, doi:10.1029/2012GL053320.

——, ——, ——, and ——, 2014: Seasonal variation of the M_2 tide. *Ocean Dyn.*, **64**, 159–177, doi:10.1007/s10236-013-0679-0.

Munk, W., and C. Wunsch, 1998: Abyssal recipes II: Energetics of tidal and wind mixing. *Deep-Sea Res. I*, **45**, 1977–2010, doi:10.1016/S0967-0637(98)00070-3.

Olbers, D., J. Willebrand, and C. Eden, 2012: *Ocean Dynamics.* Springer Verlag, 704 pp., doi:10.1007/978-3-642-23450-7.

Polzin, K. L., and Y. V. Lvov, 2011: Toward regional characterizations of the oceanic internal wavefield. *Rev. Geophys.*, **49**, RG4003, doi:10.1029/2010RG000329.

Ray, R. D., and G. T. Mitchum, 1997: Surface manifestation of internal tides in the deep ocean: Observations from altimetry and island gauges. *Prog. Oceanogr.*, **40**, 135–162, doi:10.1016/S0079-6611(97)00025-6.

——, and E. D. Zaron, 2011: Non-stationary internal tides observed with satellite altimetry. *Geophys. Res. Lett.*, **38**, L17609, doi:10.1029/2011GL048617.

Saenko, O. A., and W. J. Merryfield, 2005: On the effect of topographically enhanced mixing on the global ocean circulation. *J. Phys. Oceanogr.*, **35**, 826–834, doi:10.1175/JPO2722.1.

Schiller, A., and R. Fiedler, 2007: Explicit tidal forcing in an ocean general circulation model. *Geophys. Res. Lett.*, **34**, L03611, doi:10.1029/2006GL028363.

Shriver, J. F., B. K. Arbic, J. G. Richman, R. D. Ray, E. J. Metzger, A. J. Wallcraft, and P. G. Timko, 2012: An evaluation of the barotropic and internal tides in a high-resolution global ocean circulation model. *J. Geophys. Res.*, **117**, C10024, doi:10.1029/2012JC008170.

Simmons, H. L., R. W. Hallberg, and B. K. Arbic, 2004a: Internal wave generation in a global baroclinic tide model. *Deep-Sea Res. II*, **51**, 3043–3068, doi:10.1016/j.dsr2.2004.09.015.

——, S. R. Jayne, L. C. St. Laurent, and A. J. Weaver, 2004b: Tidally driven mixing in a numerical model of the ocean general circulation. *Ocean Modell.*, **6**, 245–263, doi:10.1016/S1463-5003(03)00011-8.

Stammer, D., and Coauthors, 2014: Accuracy assessment of global barotropic ocean tide models. *Rev. Geophys.*, **52**, 243–282, doi:10.1002/2014RG000450.

Steele, M., R. Morley, and W. Ermold, 2001: PHC: A global ocean hydrography with a high-quality Arctic Ocean. *J. Climate*, **14**, 2079–2087, doi:10.1175/1520-0442(2001)014<2079:PAGOHW>2.0.CO;2.

St. Laurent, L. C., H. L. Simmons, and S. R. Jayne, 2002: Estimating tidally driven mixing in the deep ocean. *Geophys. Res. Lett.*, **29**, 2106, doi:10.1029/2002GL015633.

Thomas, M., J. Sündermann, and E. Maier-Reimer, 2001: Consideration of ocean tides in an OGCM and impacts on subseasonal to decadal polar motion excitation. *Geophys. Res. Lett.*, **28**, 2457–2460, doi:10.1029/2000GL012234.

von Storch, J.-S., C. Eden, I. Fast, H. Haak, D. Hernández-Deckers, E. Maier-Reimer, J. Marotzke, and D. Stammer, 2012: An estimate of the Lorenz energy cycle for the World Ocean based on the 1/10° STORM/NCEP simulation. *J. Phys. Oceanogr.*, **42**, 2185–2205, doi:10.1175/JPO-D-12-079.1.

Zhao, Z., M. H. Alford, and J. B. Girton, 2012: Mapping low-mode internal tides from multisatellite altimetry. *Oceanography*, **25**, 42–51, doi:10.5670/oceanog.2012.40.